Materials Technology Reports 2026, 4(1), 3996.
doi: https://doi.org/10.59400/mtr3996

Article

Investigation of optical, magnetic and antimicrobial characterization of $BaCoO_{2.6}$ nanoparticles

Fareenpoornima Rafiq[1,*], Sumathi Jones[2], Parthipan Govindsamy[1], Papitha Purushothaman[3]

[1] Department of Physics, Vel Tech Multi Tech Dr. Rangarajan Dr. Sakunthala Engineering College, Chennai 600062, India

[2] Department of Pharmacology, Sree Balaji Dental College and Hospital, Bharath Institute of Higher Education and Research, Chennai 600100, India

[3] Department of Computer Science, Dr.M.G.R. Educational and Research Institute, Chennai 600095, India

*** Corresponding author:** Fareenpoornima Rafiq, poornima7j74@gmail.com

CITATION

Rafiq F, Jones S, Govindsamy P, et al. Investigation of optical, magnetic and antimicrobial characterization of $BaCoO_{2.6}$ nanoparticles. Materials Technology Reports. 2026; 4(1): 3996.
https://doi.org/10.59400/mtr3996

ARTICLE INFO

Received: 4 February 2026
Revised: 26 May 2026
Accepted: 29 May 2026
Available online: 15 June 2026

Abstract: The research reports first on the optical properties of $BaCoO_{2.6}$ nanoparticles, using the transmission spectrum, viz., the band gap. The nanoparticle size of 25 nm with grain size ranging from 0.5 μm to 5 μm was revealed. Tauc's indirect transition model describes the optical band gap (E_g) as 5.28 eV, using which the optical features such as extinction coefficient, refractive index, and the loss function have been evaluated. The synthesized sample's average refractive index lies in the range 1.0–2.5, the Urbach energy, calculated from inter-band localized electronic states generated by defects, was found to be 2.01 eV. As the entire region does not bear any absorption band, the sample finds its suitability in NLO-SHG devices. Interesting outcomes in line with optical properties were also demonstrated by the photoluminescence properties. The electron transition at 800 nm, which is also linked to the electronic transition of Co^{2+}/Co^{3+} ions, is responsible for the peak. The electrons may be trapped at the oxygen vacancies at a tetrahedral site, or they may be caused by impurities or structural flaws in the material and may suggest a mixed phase transition. The magnetic squareness ratio being less than 0.5 emphasizes the synthesized sample's anisotropic, single-domain, soft magnetic nature. The present exploration of $BaCoO_{2.6}$ nanoparticles highlights that their antimicrobial efficacy extends well beyond conventional growth inhibition metrics such as the minimum inhibitory concentration (MIC) and the minimum bactericidal concentration (MBC).

Keywords: refractive index; transparency; Urbach energy; anti-bacterial; dentistry; anisotropy; single-domain

1. Introduction

Science and technology, optical communications, finance and commerce, entertainment, and enhancing the performance of computers and other data processing units with increased flexibility are important applications of optical spectroscopy. For a variety of applications, including absorbers, optical coatings, reflectors, and various optoelectronic devices, it is crucial to examine a material's optical properties concerning how it reacts to incident electromagnetic radiation [1,2]. Ultrafast optical switching devices are the main components of next-generation broadband technologies. The optical switching devices must be implemented using materials with minimal linear loss. Due to their desired functionalities, low cost, and versatile chemical stability,

as well as their unique optical, catalytic, electrical, and adsorption properties, metal oxide nanomaterials have also significantly accelerated biosensing research in recent years [3]. These properties offer an appealing platform for connecting biomolecules, such as antibodies, nucleic acids, enzymes, and receptor proteins, as sensing elements to the transducer for signal detection or amplification [4]. The NIR area of biomedical imaging has garnered significant attention due to the reduced scattering and absorption of light by tissues at longer wavelengths, facilitating deeper penetration into biological tissues compared to visible light. The use of luminescent labels in biological applications, especially biomedical imaging, has become widespread. The creation of luminous nanophosphors with excitation/emission maxima that fall in the region of minimal tissue absorbance, enabling deeper penetration depth with high imaging contrast, has received a lot of interest recently [5,6].

Cobalt oxide has attracted a lot of attention lately because of its accessibility, ease of synthesis, abundance, and environmental friendliness. Furthermore, compared to lead, mercury, and nickel, all of which are still utilized in the energy sector, cobalt oxide is significantly less hazardous. The electrochemical properties of metal oxides are typically associated with flaws in the crystal lattice. Cobalt oxide was discovered to have the biggest figure of merit, that is, the ratio of the optical nonlinearity to the linear optical absorption, among those transition metal oxides. The most stable phase in the Co-O system is cobalt oxide [$Co^{2+}(Co^{3+})_2O^4$], a mixed-valence compound with a typical spinel structure where Co^{2+} and Co^{3+} are arranged at tetrahedral and octahedral sites, respectively. A change in shape, an increased band gap, and an oxygen vacancy caused by doping Co_3O_4 with barium metal highlight the significance of the charge transfer mechanism in photocatalytic activities [7]. The nanoparticles (NPs) with oxygen vacancies promoted lattice expansion (structural regularity modification), which redshifted the band gap and changed the material's visible luminescence [8].

Two categories can be used to describe the absorption process in the photon-electron interaction. In the first type, the photon is absorbed and advances to a higher state when its frequency coincides with that of the excited electron. In the latter group, the material becomes transparent to the incident radiation. The fundamental absorption in the medium is caused by an excitonic process or a band-to-band transition during the photon's interaction with the substance. The interaction of valence band electrons and photons with subsequent excitation into the conduction band across the fundamental absorption edge of crystalline and non-crystalline materials is referred to as a direct or indirect band transition [1, 9]. Furthermore, indirect transitions also involve concurrent interaction with lattice vibration. In the fields of semiconductors, nanomaterials, and solar energy, the analysis of the forbidden energy gap, the lowest energy required for these transitions, is essential. The bandgap of semiconductors is smaller (<3 eV), and that of insulators is larger (>4 eV). In addition, solar operations monitor the bandgap, the area of the solar spectrum that the photovoltaic cell absorbs as it travels to Earth. When the bandgap of the nanomaterial is greater than the bandgap of the solar spectrum, the energy gap must be controlled for the solar cell to be as efficient as possible and to minimize heat loss [10].

Anisotropy, temperature, and pressure are some of the factors that influence a

crystalline material's bandgap (E_g) when exposed to an electromagnetic field [11]. Several optical devices, including low-loss waveguides, resonators, distributed Bragg reflectors, photonic crystals, LEDs, passive splitters, biosensors, attenuators, filters, and resonators, operate depending on the presence of interstices, a small number of oxygen vacancies, and electrical insulators with low refractive index and low absorption [12].

The flexible oxygen stoichiometry and modifiable non-precious transition metal oxidation states of barium-cobaltate-based perovskite ($BaCoO_{3-\delta}$) and barium-cobaltate-based nanocomposites have led to extensive research on energy storage and conversion devices. Depending on the oxygen stoichiometry, many polymorphs have been described, ranging from the modified 12H-hexagonal and 5H-trigonal to the hexagonal $BaCoO_{3-\delta}$ perovskite phase for oxygen-rich compositions, while the end-member trigonal $BaCoO_2$ and a notably oxygen-deficient $BaCoO_{2.2}$ cubic perovskite structure were considered as the reduced phases. When oxygen is inserted into the BCO phase, the co-oxidation state gradually changes from 3+ to 4+. The precise temperature of this transition and the coexistence of several phases are difficult to determine and further research is significant [13].

Strong electron correlations and magnetic interactions cause spin-dependent transport phenomena in materials like nickelates ($NdNiO_3$) and cobalt oxides ($SrCoO_3$). The coupling of charge, spin, and lattice degrees of freedom accounts for these materials' significant Seebeck coefficients and metal-insulator transitions [14]. Mixed valences of +2 and +3 revealed significant variations in magnetic interaction and carrier density, for which an abrupt change in both the magnetic susceptibility and the Seebeck coefficient was observed [15]. One special effect of magnetic nanoparticles is superparamagnetism. Only when the size and number of domains in a magnetic substance are both sufficiently small can superparamagnetism be seen; depending on the material's particle size, with a diameter between 10 and 150 nm.

In our earlier study, we reported on the phase transition during the synthesis process of $BaCoO_{2.6}$ and to our knowledge, the optical and magnetic properties and antimicrobial activities of the synthesized sample, $BaCoO_{2.6}$, are disclosed for the first time, and further research will be pursued. Table 1 displays the available reported data on the energy gap of barium oxide, cobalt oxide, and barium cobalt oxide nanoparticles and thin films.

Table 1. Indexed (hkl) and d-spacing of prominent peaks of the XRD pattern of $BaCoO_{2.6}$.

2θ (degree)	Relative intensity (%)	(hkl)	d-spacing (A^0)
26.13	61	106	3.42
28.11	73	107	3.13
31.32	100	110	2.83
41.52	43	206	2.17

2. Materials and methods

2.1. Synthesis of nanoparticles

All of the chemicals, $Ba(NO_3)_2$ and $Co(NO_3)$ (Sigma Aldrich), required for the synthesis were utilized without any purification and were commercially available

with a purity of at least 99%. In a stoichiometric composition of $Ba_3Mg_{3-x}Co_4O_9$, the nanocrystalline sample, $BaCoO_{2.6}$, was prepared using the citrate-nitrate sol-gel process. The mixture was stirred at 80 ℃, continued at 700 ℃ for 5 h, and finally at 900 ℃ for 2 h. The obtained black powder was ground and pelletized at 1 GPa for further characterization [16].

2.2. UV analysis

After dissolving the black powder sample in deionized water, it was sonicated. The absorbance of the solution was then measured after it was placed in a cuvette and exposed to UV-visible light. Lambert-Beer's law (Equation (2)) states that as sample concentration, path length, and molar extinction coefficient increase, the incident light intensity within the sample cell decreases exponentially [17].

As illustrated in **Figure 1**, a solvent-filled cell is placed in the measuring light beam's path, and the light beam's intensity (I_0) is measured after it passes through the cell. The intensity of the light beam (I) is then measured after it passes through a cell that contains a solution made by dissolving the sample in the solvent. Equations (1) and (2) provide the transmittance (T) and the absorbance (A), which is more frequently used with solution samples.

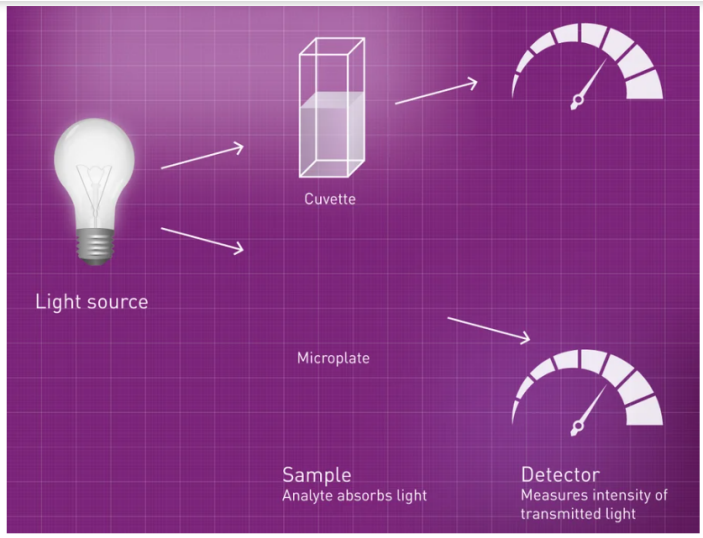

Figure 1. Measurement principle for solution samples.

$$T = \frac{I}{I_0}, \tag{1}$$

$$A = Log10\,\frac{1}{T} = \alpha cl, \tag{2}$$

$$\alpha = \frac{2.303\,A}{l}\,. \tag{3}$$

Where (α) is the sample's absorption coefficient, (c) is the sample concentration, and (l) is the cell's optical path length. With this measuring technique, only the absorption caused by the sample is determined, as it removes the effects of reflection from the cell surface and solvent absorption. The absorption value was increased as a

result of the high concentration. To analyze the optical characteristics of the prepared sample, the solution was diluted, and the absorption spectrum, depicted in **Figure 2**, was obtained.

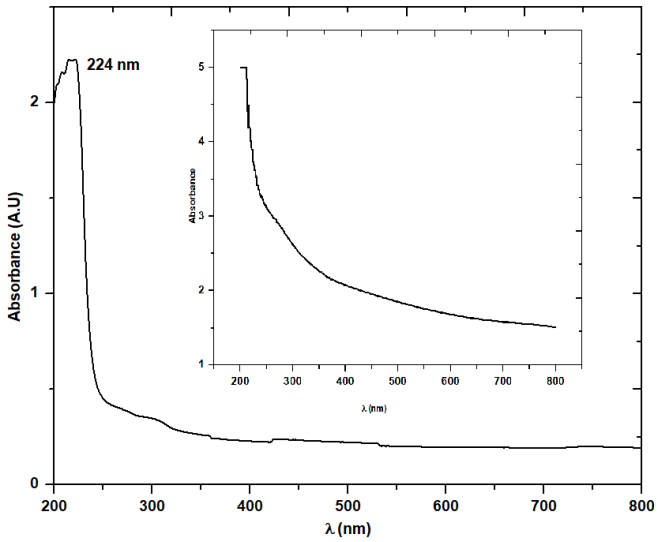

Figure 2. Absorbance spectra of diluted $BaCoO_{2.6}$ solution; Inset: concentrated $BaCoO_{2.6}$ solution.

2.3. Evaluation of optical and magnetic properties

Room-temperature optical transmittance testing of the synthesized sample was performed using a UV + t90 spectrometer, photoluminescence measurements with a Spectrofluorimeter–PerkinElmer LS 45, and a vibration sample magnetometer (VSM-Lakeshore VSM 7410S) for magnetic studies. Origin 8.6 software was used for the graphical analysis.

2.4. Antimicrobial activity against oral and environmental pathogens

Antibacterial and antifungal activity was carried out through an agar diffusion assay, and the minimum inhibitory concentration was observed against common oral pathogens, *Streptococcus mutans (S.mutans), Staphylococcus aureus (S.aureus) and Candida albicans (C.albicans*) and reactive oxygen species assay through DPPH scavenging assay [18].

3. Results and discussion

Though several methods have been adopted for the synthesis of $BaCoO_{3-\delta}$ using $BaNO_3$ and $CoNO_3$ (600 °C: 12 h, 900 °C: 10 h) and $BaCO_3$, Co_3O_4 precursors (≈1,200 K, 2 days), this is the first study to synthesize nano powder $BaCoO_{2.6}$ using the sol-gel method with a lesser annealing time. Major peaks were associated with the $BaCoO_{2.6}$, specified by its reflection planes, in concurrence with the preceding reports (JCPDS01-071-2453**)** and are displayed in **Figure 3**. The compound $BaCoO_{2.6}$ becomes crystalline in the space group P63/mmc symmetry, with the average crystallite size of the most intense peak (110) plane of $BaCoO_{2.6}$ was found to be approximately 25.26 nm. **Table 1** displays (hkl) and d-spacing of prominent peaks of the XRD pattern of $BaCoO_{2.6}$. The SEM image (**Figure 3**) with different magnifications and

the images revealed the grains in the range of 0.5–5 μm [16]. To the best of our knowledge, the optical, magnetic, and antimicrobial characteristics of the synthesized sample, $BaCoO_{2.6}$, are disclosed for the first time.

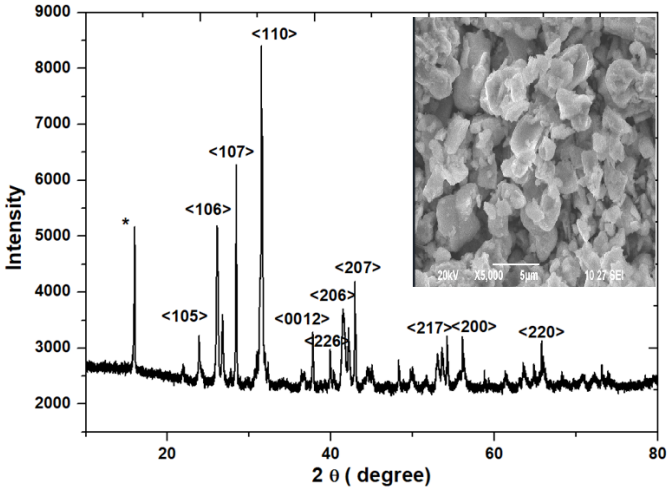

Figure 3. XRD pattern with hkl planes of intense peaks, and the inset displays the SEM image of $BaCoO_{2.6}$.

3.1. Phase transition during the synthesis procedure

During our synthesis procedure, phase transitions were observed, and only a limited list of effective compounds with verified crystal structures has been fully characterized, according to more recent findings. From 973 K to 1,173 K, the phase sequence undergoes a series of phase changes ($BaCoO_{2.6}$→$BaCoO_3$→ $Ba_3Co_2O_6(CO_3)_{0.6}$). At annealing temperatures of 623 K and 773 K, there was very little visible phase of barium cobaltite. The diffraction peak of (e) is greater than the diffraction peak of (f) when we compare the plots' e and f, suggesting that F(e) has more crystallization than (f) [19, 20]. Therefore, it is reasonable to conclude that the start-up temperature for the synthesis of $BaCoO_{2.6}$ is 750 °C and $Ba_3Co_2O_6(CO_3)_{0.6}$ is 900 °C.

Figure 4 depicts the XRD patterns of the different phases of the synthesized sample with the reported data.

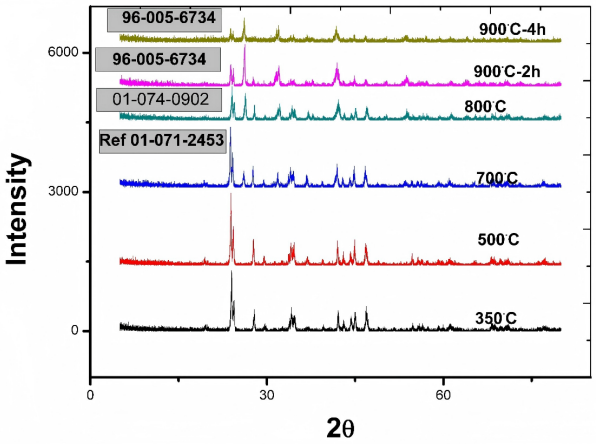

Figure 4. XRD representing different phases of the synthesized sample at different temperatures.

3.2. Optical characterization

The simplest way to determine the electronic structure of a solid is to analyze its optical absorption. Absorbance (A) is defined as the ratio of the intensity of light incident on it (I_0) to the intensity of light absorbed (I_A) [21]. Measurement of optical absorption, particularly the absorption edge, is essential to study optically induced transitions and to learn about the band structure and energy gap of non-crystalline materials [22]. Equation (2) was utilized to compute the absorbance by developing its inverse relation (Equation (2)) based on the optical transmission spectra of the nanocrystalline powder sample that were obtained in the range of 190 nm to 1,000 nm.

The absorption coefficient (α) is determined from Equation (3) [23]. The synthesized sample has an optical cut-off wavelength of 224 nm (**Figure 2**), a short cut-off edge, and a moderate transparency range extending into the visible and NIR regions.

The energy gap (E_g) can be determined from the Tauc's plot ($\alpha h\nu$ vs. $h\nu$) with the relation (4),

$$\alpha h\nu = A(h\nu - E_g)^{\beta}, \quad (4)$$

where, A is a constant, ν is the transition frequency, and the exponent (β) characterizes the nature of band transitions, wherein β = 1/2 & 3/2 corresponds to direct allowed and directly forbidden transitions and β = 2 & 3 to indirect allowed and forbidden transitions, respectively. Using the best straight-line fit with β = 2 for the indirect transition, the Tauc plot in **Figure 5** [22] is extrapolated to $h\nu$ = 0. It reveals a large energy gap (E_g) of 5.28 eV, arising from the wide transparency in the visible region [23–25]. The transparency of the sample plays an important role in the field of optical fabrication and optical signal processing. As the entire region does not bear any absorption band, the sample finds its suitability in NLO, SHG devices [26]. The sample's wide energy gap makes it suitable for solar-cell applications and dielectric filters, as short-circuit current can be increased for low window absorption loss or their capability of inserting or extracting charge carriers (**Table 2**) [27,28]. The transmission of visible and infrared radiation through the roofs helps to keep the poultry areas warm in cold countries [29].

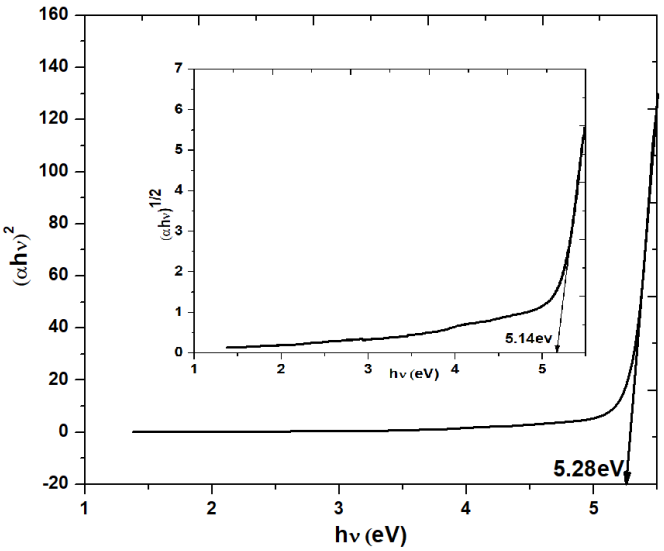

Figure 5. Tauc's direct energy and indirect, inset: Band gap of $BaCoO_{2.6}$.

Table 2. Energy gap values of some of the compounds reported so far.

Compound name	Energy gap values (eV) (direct)	Energy gap values (eV) (indirect)	References
$Co_3O_{4\ NPs}$	2.40	2.13	Basha et al. [30]
Co_3O_4 Thin film	2.0	1.0	Pawar et al. [31]
BaruimSodium Borate/Co_3O_4 glass	3.50	3.40	Taha and Abouhaswa [32]
BaO NPs	3.7	-	Naz and Saeed [33]
Cobalt oxide NPs	-	3.75	Elsammani and Hamza [34]
$BaCoO_3$	2.9	2.8	Faizee et al. [35]
$Ba_3Co_2O_6(CO_3)_{0.6}$	3.12	-	Rafiq et al. [36]

Temperature, pressure, and anisotropy, as well as microstructural elements such as short-term coordination, nano- and micro-crystallites, all influence the energy gap of crystalline materials in the application of electromagnetic forces [36,37].

It is evident from **Figure 5** that absorption is minimal at low energies. This reveals that there is not much chance of an electron transition since the input photon's energy is insufficient to transfer the electron from the valence band to the conduction band ($hv < E_g$).

At high energies, absorption is greater, indicating a greater possibility for electron transitions. The energy of the incident photon is sufficient to transfer the electron from the valence band to the conduction band, pointing to the fact that the energy of the incident photon is greater than the forbidden energy gap. This demonstrates how the absorption coefficient helps determine the type of electron transition. When the absorption coefficient is high ($\alpha > 10^4$) cm^{-1} at high energies, it is expected that a direct electron transition will occur, with the electrons and photons maintaining the energy and momentum. Conversely, when the absorption coefficient is low ($\alpha < 10^4$) cm^{-1} at low energies, it is expected that an indirect electron transition will occur, with the photon helping to maintain the electronic momentum.

The synthesized sample has an absorption coefficient less than 10^4 $cm^{-1,}$ affirming an indirect band transition. **Figure 6** shows the absorption coefficient variation with wavelength. The closeness of the sample's indirect band gap and direct band gap transition may be due to the anisotropic nature caused by the disordered layer of the CoO_6 column of the synthesized sample or may be due to the multiple optical processes paving the way for absorption [34,38–40].

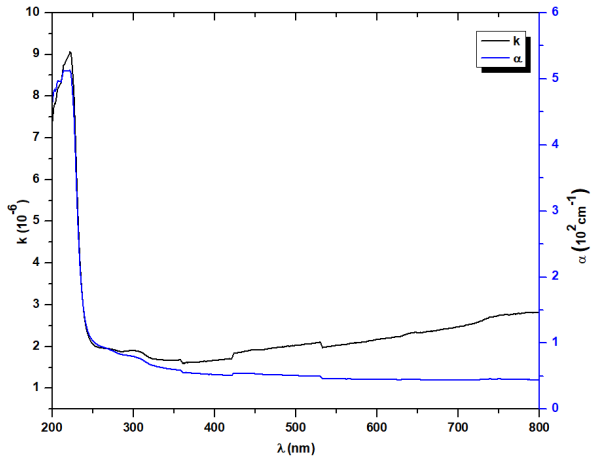

Figure 6. Relationship of absorption coefficient and extinction coefficient with wavelength.

The ratio,

$$\frac{\alpha\lambda}{4\pi} = k, \tag{5}$$

which is used to determine the extinction coefficient (k), which is a measure of the fraction of light lost owing to scattering per unit distance of the propagating medium. **Figure 6** depicts the change in k in response to wavelength. The shape consistency of (k) spectra with respect to (α) reflects the direct proportionality of the extinction coefficient to the absorption coefficient [41]. The low values of absorption and extinction coefficient values indicate the transparent nature of the sample [42–44].

The index of refraction (n) is the ratio of the speed of light in a vacuum to that of the speed in the material that does not absorb that light. The application of integrated photonics and nano-imaging relies extensively on the modifications of the refractive index, and hence on using the relation given by Equation (6) [23,28]:

$$n = \frac{1+\sqrt{R}}{1-\sqrt{R}}, \tag{6}$$

where reflectance is calculated using the formula (Equation (6)) [45,46]:

$$R = 1 - (Te^{A})^{2}. \tag{7}$$

The experimental average value of (n) of the synthesized sample is found to be in the range 1–2, as depicted in **Figure 7**.

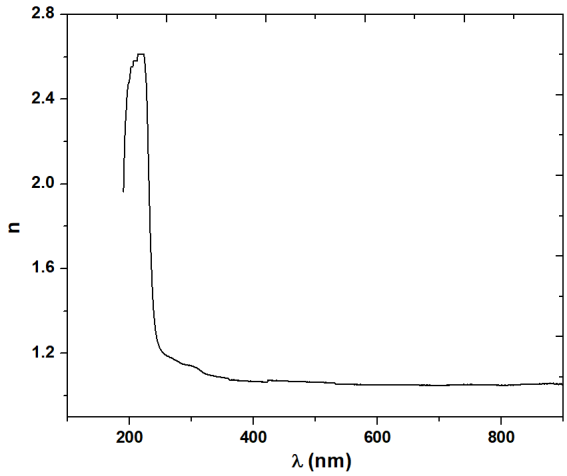

Figure 7. Variation of refractive index with wavelength.

Theoretically, the Herve–Vandamme formula [7,47,48] was used to evaluate the refractive index of the $BaCoO_{2.6}$ powder sample using Equation (8) and was found to be 1.86.

$$\left[\sqrt{1+\left(\frac{P}{E_g+Q}\right)^{2}}\right], \tag{8}$$

with P = 13.6 eV and Q = 3.4 eV as standard constant values.

The resonance effect between the input photon and these electrons' polarization is what causes the refractive index to rise as photon energy increases [49, 50]. As

the wavelength increases, the refractive index decreases, displaying typical dispersion behavior that could be caused by an increase in transmittance [25,51,52]. The photon being caught in the grain boundaries or consecutive internal reflections could be the cause of the low value of (n) [16,29,53]. Given the close correlation between (n) and the band gap energy, it can be deduced that materials with a wider band gap have smaller values of (n) [52].

The electrical insulator materials with low refractive index and low absorption are needed for various optical devices, such as low loss waveguides, resonators, photonic crystals, distributed Bragg reflectors, light-emitting diodes, passive splitters, biosensors, attenuators, and filters [38,53–56]. These low values of n may be caused by the existence of few oxygen vacancies. It is well known that the refractive index is affected by crystallinity, electronic band structure, and lattice point defects [12].

Optical conductivity (σ_0) means the conductance of charge carriers due to optical excitation in the material, and its value describes the strength of the irradiating light [57]. The relation between the conductivity and photon energy is displayed in **Figure 7**.

$$\sigma_0 = \frac{\alpha n c}{4\pi}, \tag{9}$$

where α, n and c are the absorption coefficient, refractive index, and speed of light, respectively. The conductivity rises significantly near the bandgap energy value (≅5.1 eV), attributing it to the photon-electron interaction [40], and the highest value is 3.2 $\times 10^{11}$ S^{-1} at 5.6 eV. At increasing photon energy, optical conductivity increases. This could be because the sample in that region is highly absorbent or the photon energy excites the electrons [58].

Figure 8 clearly illustrates how the absorption coefficient and the material's refractive index directly affect optical conductivity. The material's impressive photo sensitivity is confirmed by its low extinction coefficient (10^{-6}) and high optical conductivity (10^{11}) [10].

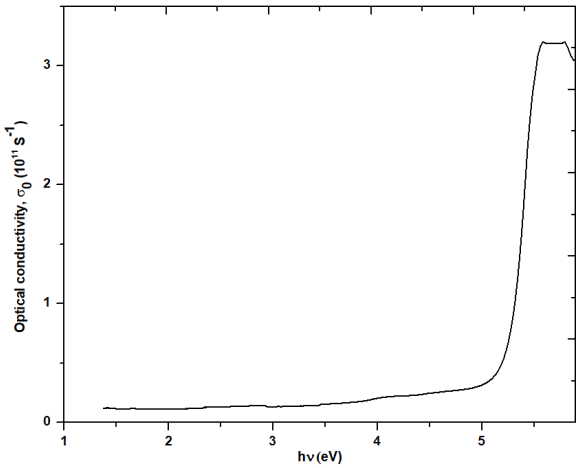

Figure 8. Optical conductivity variation with photon energy.

The material's inclination toward metallicity and insulating properties is expressed by the metallization criteria (M) given by relation 8, which is less than 1, indicating the sample's non-metallic nature and its suitability as a probe for non-linear optical

materials [56]. The existing result is in correlation with our previous findings of the metal-insulator transition [16].

$$M(E_g) = \frac{\sqrt{E_g}}{20} = 0.512. \tag{10}$$

Any fast-moving electrons that pass through the material lose energy as a result of either absorbing energy in a single electron transition or the cumulative effects created within the material. The imaginary part (ε_i) of the dielectric constant describes how a dielectric absorbs energy from an electric field due to dipole motion, while the real part (ε_r) shows how much it will slow down the speed of waves in the material. The loss factor quantifies the phase difference caused by energy loss at a specific frequency or establishes how much electromagnetic energy is lost in the medium [22, 51]. The dielectric constant's lower, positive value demonstrates that the sample is suitable for use in optoelectronic devices and shows that the material can induce polarization due to incident electromagnetic radiation, thereby enhancing optical properties [52].

The dielectric constants were used to calculate the energy loss of the material using Equations (11) and (12) and depicted in **Figure 9**.

$$\varepsilon_r = n^2 - k^2, \tag{11}$$

$$\varepsilon_i = 2nk, \tag{12}$$

where *k* represents the extinction coefficient.

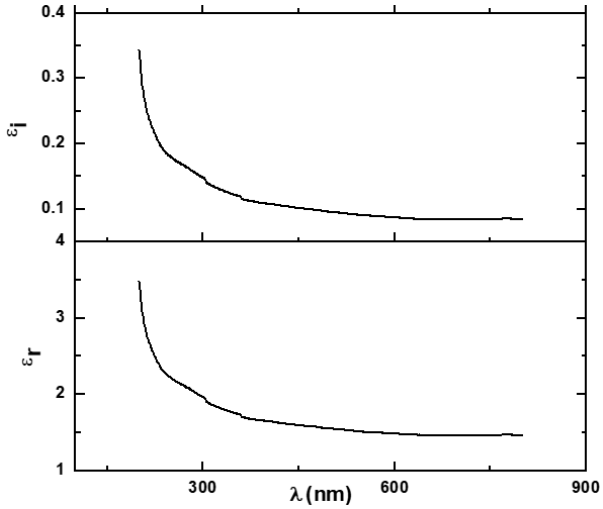

Figure 9. Response of the real and imaginary parts of the dielectric constant to wavelength.

3.3. Determination of Urbach energy (E_u)

Urbach energy results from the absence of an orderly arrangement of atoms in the material, wherein the valence and conduction bands do not have sharp cut-offs but instead have tails representing the localized density of states [15, 25]. Because of this, the absence of a straight line at lower energies in Tauc's plot and the tailing off of the absorption coefficient, α, in an exponential manner is noticed. This tail of ρhv extending into the energy band gap is termed the Urbach tail, and the energy associated with this tail is referred to as the Urbach energy. It relies on temperature,

thermal vibrations, static and induced disorder, strong ionic bonds, average photon energies, etc., and is used to review the change in bandgap and inter-band formation. E_u quantifies the steepness of the absorption starting at the band edge and, hence, the extent of the density of states. A stronger absorption initially indicates a lower Urbach energy [56]. It is thought that random fluctuations in internal fields linked to structural disorder are the cause of the exponential dependency of (α) on energy ($h\nu$). Electronic transitions between localized states could be the source of it.

The values of Urbach energy decrease as the energy gap widens, suggesting a lesser defect content [54,56].

Equation (13) represents the Urbach empirical rule, which expresses the spectrum dependence of the absorption coefficient α ($h\nu$) on photon energy ($h\nu$):

$$\alpha h\nu = \alpha_0 \exp\left(\frac{h\nu}{E_u}\right). \tag{13}$$

Due to localized states in the band gap of disordered or low-crystalline materials, this energy is frequently accessed as the width of the band tail and is weakly temperature dependent [57,58].

Taking the log on both sides and applying the fundamental laws of logarithms,

$$ln(\alpha h\nu) = lnB + \frac{h\nu}{E_u}, \tag{14}$$

simplifying,

$$ln(\alpha h\nu) = \frac{h\nu}{E_u} + \text{constant}. \tag{15}$$

Using the equation of a straight line,

$$y = mx + c, \tag{16}$$

and by scaling *Ln(α)* vs. $h\nu$ (**Figure 10**), wherein the reciprocal of the slope of the linear region yields the value of E_u of the localized state of the bandgap. The value of E_u is found to be 2.01 eV.

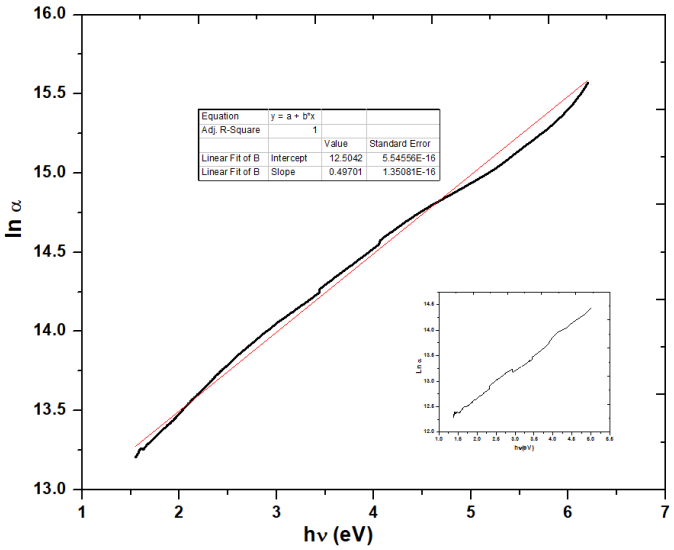

Figure 10. Urbach energy plot of $BaCoO_{2.6}$—slope of the inset graph.

3.4. Photoluminescence (PL) studies

PL spectra are a simple and useful tool for examining how morphology affects a sample's electrical, optical, and photochemical characteristics to elucidate the energy band structure and defect states in nanoparticles with emission/excitation power to quantum efficiency. **Figure 11** shows the photoluminescence spectra of the synthesized sample at two excitation wavelengths of 280 nm and 400 nm. The graph shows two sharp emission peaks at 333 nm in the visible region and 800 nm in the near-IR region, respectively. The spectrum showed a strong emission in the visible region, indicating that the sample had good crystallinity.

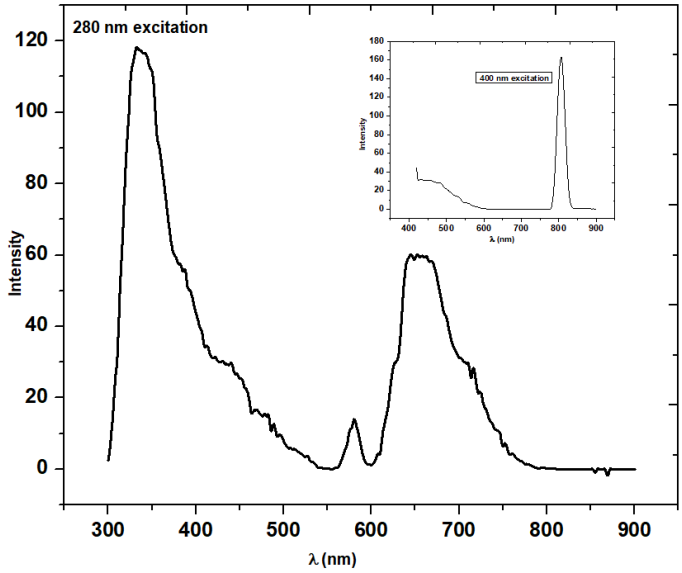

Figure 11. Photoluminescence spectra of $BaCoO_{2.6}$ at an excitation wavelength of 280 nm; Inset: Excitation wavelength of 400 nm.

The presence of defects, such as singly ionized oxygen vacancies caused by impurity phases in the synthesized sample, is responsible for the green emission band seen at 533 nm [59, 60]. The PL emission was strong because of the greater rate of recombination between excited holes and ionized oxygen vacancies [61]. Annealing improves oxygen-related defects, which may be the cause of the PL band's varied intensity, as it physically removes oxygen-vacancy states [49]. As the excitation wavelength increases (from 280 nm to 400 nm), the strength of the asymmetric bands or the intensity of the peak in the PL spectra decreases. Additionally, because there are several emissive centres, the place of maximum is redshifted as the excitation wavelength increases [62]. The electron transition at 800 nm, which is also linked to the electronic transition of Co^{2+}/Co^{3+} ions, is responsible for the peak. The electrons may be trapped at the oxygen vacancies at a tetrahedral site, or they may be caused by impurities or structural flaws in the material [55, 62] and may suggest a mixed phase transition, as per the reports [61]. Our earlier research work suggested that the sample has a mixed-phase transition [16]. One simple method to alter the concentration of surface oxygen vacancies is to anneal in an environment that is rich in oxygen. Oxidation in air has the effect of physically eliminating locations where oxygen vacancies exist. Vacancies associated with surface oxygen defects can have

a major impact on the material's photocatalytic and PL properties [63]; the shifting of wavelengths to the NIR region finds solar cell-based application prospects [64], and emission between 750 and 1,200 nm may be particularly useful for tracking drug delivery mechanisms in the near-infrared spectrum [5].

Recent research shows the applications of the NIR region in tissue penetration for luminescent nanoprobes [65, 66]. Our future study will be the sample probe in biomedical imaging.

3.5. Magnetic property analysis

The magnetic property involves the investigation of the M-H curve using a vibration sample magnetometer (VSM) to compute the magnetic parameters, such as saturation magnetization (M_s), remanence (H_r), and coercivity (H_c). The change of magnetization (M) as a function of the applied field (H) at room temperature for the sample $BaCoO_{2.6}$ is portrayed in **Figure 12**. The magnetization (M) increases with increasing applied field (H), without saturation due to the anisotropic nature, and shows a narrow hysteresis loop with less dissipation of heat, similar to soft magnetic materials. The anisotropic single-domain superparamagnetic material is suitable for biomedical applications [66–69]. A squareness ratio below 0.5 indicates the sample's single-domain nature. The composition, preparation technique, crystallite size, and cation distribution at the A and B sites all affect the hysteresis loops' width and shape. When the size of magnetic materials is reduced below the single-domain limit and the coercivity and remanence reach zero, superparamagnetism takes place, allowing the magnetic moments to freely rotate and quickly change direction. Consequently, the particle's net magnetization is zero when there is no magnetic field. Neel and Brownian relaxation mechanisms cause SPIONs to release heat when an alternating magnetic field (AMF) is applied. The Brownian relaxation process is linked to the viscosity of the fluid in which the nanoparticles are suspended, whereas the Neel relaxation mechanism is connected to magnetocrystalline anisotropy [67]. The study of domain structure and the dissipation of energy is important for the design of thermal sensing devices [70–72]. The values of M_s, H_r, and H_c are tabulated (**Table 3**).

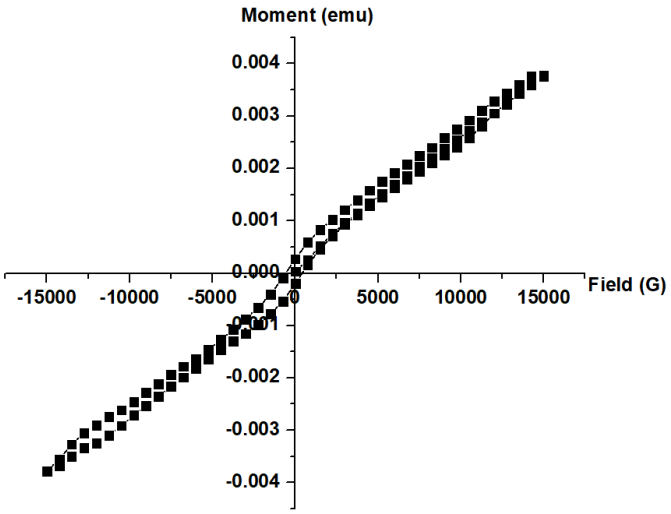

Figure 12. Hysteresis loop of $BaCoO_{2.6}$.

Table 3. Magnetic parameters of $BaCoO_{2.6}$.

Saturation magnetization (M_s) emu	Coercivity (H_c) G	Remanence (M_r) emu × 10^{-3}	M_r/M_s (no unit)
3.78	491.73	235.81	0.0624

3.6. Anti-microbial and antioxidant studies

Application of $BaCoO_{2.6}$ nanoparticles in dentistry and bioremediation

The results clearly indicate that the synthesized nanoparticles possess antimicrobial activity against all three microbes. The inhibitory potential is dose-dependent. The minimum inhibitory concentration for *Streptococcus mutans* is 1.5 mg/mL, *Staphylococcus aureus* is 2.2 mg/mL, and *Candida albicans* is 2.5 mg/mL (**Figure 13**).

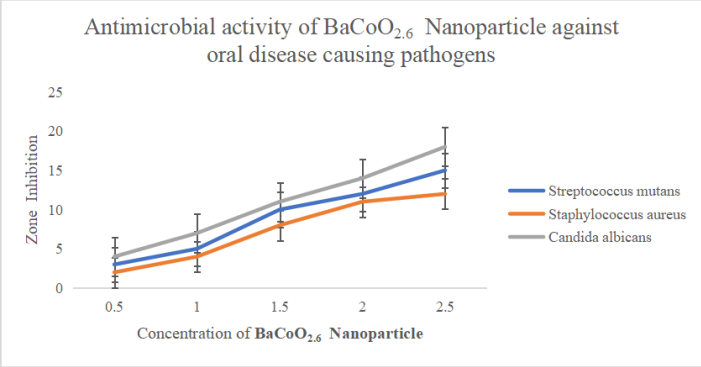

Figure 13. Antimicrobial activity of nanoparticle $BaCoO_{2.6}$.

Nanoceramics are primarily oxides, phosphates, carbides, and carbonates of metals and metalloids that possess distinct mechanical, electrical, optical, and magnetic properties.

Nanoceramic oxide paves the way for medical, dental, and biomedical applications in the diagnosis, treatment, and prevention of various diseases. The quality of treatment and products used in dentistry can be enhanced by nanoparticles. The denture-fixed oral mucosa is deficient in oxygen supply and saliva, which are the major contributors to microbial overload.

Prosthetic dentistry aims at replacing missing teeth with implants and fixed and removable dentures. Nanomaterials that include metal nano oxides have been proven successful as prosthetic products as they increase mechanical properties, including tensile strength and durability.

Chronic denture use and poor oral hygiene are the major causes of microbial infections. Moreover, the type of denture material strongly influences biofilm development. Most pathogenic microorganisms causing oral dental infections are *Streptococcus mutans (MTCC 890*), *Staphylococcus aureus*, and *Candida albicans* (MTCC 854). Candida may cause mild, moderate, to severe infections, which may be fatal.

In dentistry, candidiasis is the most common infection seen in immunocompromised individuals and is classified based on the location as oropharyngeal or esophageal candidiasis. *C.albicans* destroys the host tissue

through the release of hydrolytic enzymes, thereby damaging the cell membrane and targeting the host immune mechanism [73–76].

Earlier studies incorporating nano oxides TiO_2, ZrO, and ZnO in prosthetic materials have enhanced mechanical properties. Additionally, nanomaterials with antimicrobial activity are an added advantage in the field of dentistry [77–79].

Nano oxide has a minimal negative impact on the environment and is maximally utilized in heavy metal pollution. Enzymatic nanoparticle remediation is gaining interest in bioremediation processes. Wastewater contains many organic and inorganic compounds and microorganisms, resulting in an increase in chemical and biological oxygen demand. The synthesized nanoparticle inhibits the growth of E.coli (MTCC 579), the most prevalent microbe present in sludge and wastewater.

Nanoparticles find application as biosensors in the detection and destruction of both heavy metal and pesticide toxicity. Nanophyto-remediation has been found effective in counteracting the potential danger associated with organochlorine compounds (endosulfan). NANOREM (Nanotechnological remediation from lab scale to end-user application for the restoration of a clean environment) is a recent advancement in bioremediation. Nanotechnological remediation processes from Lab Scale to End User Applications for the Restoration of a Clean Environment (NANOREM) are fabricated to expose the unexplored area of nano-remediation and support sustainable development [80].

The present study demonstrates that $BaCoO_{2.6}$ nanoparticles exhibit significant antimicrobial effects against major oral pathogens such as *S.mutans, S.aureus, and C. albicans,* highlighting their potential in preventing and managing oral infections. In comparison to conventional agents like chlorhexidine and antifungals, which face limitations due to side effects and resistance, $BaCoO_{2.6}$ Nanoparticles possess broad-spectrum activity with antibiofilm and reduced antimicrobial resistance [78, 79]. The mechanism underlying the antimicrobial activity of $BaCoO_{2.6}$ is the generation of reactive oxygen species (ROS). Upon interaction with aqueous or biological environments, they will undergo hydrolytic decomposition, resulting in the production of hydrogen peroxide (H_2O_2) and other highly reactive intermediates, such as hydroxyl radicals, superoxide anions, and reactive oxygen species. ROS production will induce oxidative stress within microbial cells and leads to lipid peroxidation, protein oxidation, and nucleic acid damage. Such oxidative stress will alter essential cellular processes, including DNA replication and enzymatic activity, leading to microbial cell death. This ROS-mediated mechanism aligns with nanotoxicological paradigms, where oxidative stress serves as a central determinant of nanoparticle-induced antimicrobial effects [80].

The synthesized nanoparticle exhibited DPPH radical scavenging activity. The inhibition percentage increased from 19.4 ± 1.3 at 25 (µg/ml) to 80.4 ± 1.4 at 400 (µg/ml). However, the activity remained lower than the standard ascorbic acid at 400 (µg/ml). The IC_{50} value of $BaCoO_{2.6}$ nanoparticles was 110 ± 1.5 compared to 38 ± 1.8 of the standard, indicating moderate antioxidant activity, as tabulated in **Table 4**.

Table 4. DPPH free radical scavenging antioxidant activity of $BaCoO_{2.6}$ nanoparticle.

Concentration (µg/ml)	$BaCoO_{2.6}$ nanoparticle	Ascorbic acid (% inhibition)
25	19.4 ± 1.3	40.8 ± 1.2
50	32.6 ± 1.2	59.3 ± 1.1
100	48.2 ± 1.7	69.9 ± 1.4
200	64.2 ± 1.5	83.9 ± 1.8
400	80.4 ± 1.4	91.8 ± 1.7

The antioxidant activity may be due to cobalt cycling, surface-mediated electron transfer, and reactive oxygen species scavenging mechanisms.

Additionally, due to oxidative damage, $BaCoO_{2.6}$ nanoparticles exert direct effects on the integrity of microbial membranes. The nanoscale dimensions will facilitate close interaction with bacterial cell envelopes through electrostatic attraction to negatively charged membrane components. This interaction, coupled with ROS-induced lipid peroxidation, will disrupt membrane architecture, increase permeability, and lead to leakage of intracellular constituents such as ions, proteins, and adenosine triphosphate (ATP). The loss of membrane potential and structural integrity further enhances cell death, thus emphasizing membrane disruption as a critical complementary mechanism. Such intracellular targeting enhances antimicrobial efficacy, particularly against Gram-negative bacteria, which possess comparatively thinner peptidoglycan layers [80]. The formation of an alkaline microenvironment due to the generation of represents an additional antimicrobial pathway. Elevated local pH conditions can denature microbial enzymes, disrupt metabolic pathways, and inhibit the growth of acidogenic and aciduric organisms. This mechanism is particularly relevant in the context of oral pathogens, where acid-producing bacteria play a central role in disease progression. This property is especially beneficial in targeting biofilm-associated infections, where hypoxic microenvironments often limit the efficacy of conventional antimicrobial agents.

Despite these promising antimicrobial properties, the potential cytotoxic effects on host cells cannot be overlooked. Excessive ROS generation may induce oxidative stress in mammalian cells, leading to mitochondrial dysfunction, apoptosis, or necrosis. Therefore, the therapeutic application of $BaCoO_{2.6}$ nanoparticles necessitates careful optimization of particle size, concentration, and surface characteristics to achieve a balance between antimicrobial efficacy and biocompatibility.

Their ability to simultaneously disrupt membranes, induce intracellular damage, and modulate local conditions positions them as promising drugs for managing resistant infections and biofilm-associated diseases. Future research should focus on surface functionalization strategies, dose optimization, and combinatorial approaches with bioactive phytochemicals to enhance efficacy while minimizing toxicity.

Previous studies suggest that ZnO, a metal-based nanoparticle, acts mainly through disruption of the membrane, release of ions, and induction of oxidative stress, which results in impaired microbial growth and decreased biofilm formation. Additionally, nanoparticles can serve as drug delivery systems for drugs and phytochemicals that enhance the stability and retention time in the oral cavity and open up new avenues for applications in dentistry as mouthwashes, varnishes, and dental materials.

However, biocompatibility, cytotoxicity, and long-term safety must be evaluated for $BaCoO_{2.6}$ to ensure applications as next-generation antimicrobial agents.

4. Conclusion

The synthesized sample, $BaCoO_{2.6}$, has been investigated for optical parameters using the synthesized sample's energy gap. The lower cut-off wavelength of 223 nm, the refractive index in the range of 1.0 to 2.0, and good transparency in the visible region have been reported. The transparency in the visible region and the wide energy gap of 5.28 eV from the Tauc's plot result in a low refractive index. The metallization parameter being less than one infers the sample's insulating property. Interband localized electronic states generated by defects through Urbach energy calculations were found to be 2.01 eV. Vacancies associated with surface oxygen defects can have a major impact on the material's photocatalytic and PL properties; the shifting of wavelengths to the NIR region opens up solar cell-based application prospects and the sample's probe in biomedical imaging. The magnetic study revealed the sample's anisotropic, soft-magnetic nature, with a single-domain structure. The microbial growth inhibitory potential of the synthesized nanoparticles can be widely used in biomedical applications. Simultaneously, the nanomaterial is being explored for the eradication of disease-causing microbes in wastewater and sludge, and for its use in bioremediation. The antimicrobial action of $BaCoO_{2.6}$ nanoparticles is due to the synergistic interplay of ROS generation, membrane disruption, intracellular cytotoxicity, alkaline microenvironment formation, and oxygen release. These comprehensive mechanistic profiles underscore their potential as next-generation antimicrobial agents for oral infections. These computations of $BaCoO_{2.6}$ nanoparticles, which have not been performed previously, would be very helpful in the search for a cost-effective, tunable material for optoelectronics and biomedical applications.

Author contributions: FR carried out the experimentation, analysis of various studies, and drafted the manuscript; SJ helped procure materials for synthesis, the bioremediation process, the discussion of results, and sequence alignment; PG supervised and helped in the drafting of the manuscript; PP helped in correlating the graphs and conceptualization. All authors have read and agreed to the published version of the manuscript.

Funding: No funding was received for this original research work.

Institutional review board statement: Not applicable.

Informed consent statement: Not applicable.

Data availability statement: The data to support the findings of the study are included in the article.

Acknowledgement: One of the authors (FR) would like to thank the Department of Physics, Loyola College, Chennai, for UV-Vis studies; the Department of Physics, St. Joseph's College, Trichy, for PL studies; the Department of Chemistry, IIT

Madras, for magnetic studies, and Sree Balaji Dental College and Hospital, Chennai, for antimicrobial analysis.

Conflict of interest: The authors declare that there are no conflicts of interest regarding the publication of this paper.

AI use statement: The authors declare that no artificial intelligence (AI) tools were used in the preparation of this manuscript.

References

1. Joudeh N, Linke D. Nanoparticle classification, physicochemical properties, characterization, and applications: a comprehensive review for biologists. Journal of Nanobiotechnology. 2022; 20(1): 262. doi: 10.1186/s12951-022-01477-8.
2. Das C, Begum J, Begum T, et al. Effect of thickness on the optical properties of Gaas thin films. Journal of Bangladesh Academy of Sciences. 2013; 37(1): 83–91. doi: 10.3329/jbas.v37i1.15684.
3. Radhakrishnan AA, Beena BB. Structural and optical absorption analysis of CuO nanoparticles. Indian Journal of Advances in Chemical Science. 2014; 2(2): 158–161.
4. Kumar P, Rajan R, Upadhyaya K, et al. Metal oxide nanomaterials based electrochemical and optical biosensors for biomedical applications: Recent advances and future prospectives. Environmental Research. 2024; 247: 118002. doi: 10.1016/j.envres.2023.118002.
5. Wang R, Zhang F. NIR luminescent nanomaterials for biomedical imaging. Journal of Materials Chemistry B. 2014; 2(17): 2422. doi: 10.1039/c3tb21447h.
6. Chen Y, Wang S, Zhang F. Near-infrared luminescence high-contrast in vivo biomedical imaging. Nature Reviews Bioengineering. 2023; 1(1): 60–78. doi: 10.1038/s44222-022-00002-8.
7. Yan X, Li Y, Zhao J, et al. Roles of grain boundary and oxygen vacancies in $Ba_{0.6}Sr_{0.4}TiO_3$ films for resistive switching device application. Applied Physics Letters. 2016; 108(3): 033108. doi: 10.1063/1.4940198.
8. Dangi R, Basnet B, Pandey M, et al. Effect of Oxygen Vacancy on the Crystallinity and Optical Band Gap in Tin Oxide Thin Film. Energies. 2023; 16(6): 2653. doi: 10.3390/en16062653.
9. Essahlaoui A, Essaoudi H, Hallaoui A, et al. Calculation of the thickness and optical constants of lead titanate thin films grown on MgO from their transmission spectra. Journal of Materials and Environmental Sciences. 2018; 9(1): 228–234. doi: 10.26872/jmes.2018.9.1.26.
10. Christuraj P, Raja MD, Madhavan J. Linear and Nonlinear Optical Properties of metal incorporated L-Serine Crystal. International Research Journal of Engineering and Technology. 2017; 4(9): 75–77. Available online: https://www.irjet.net/archives/V4/i9/Special_Issue/IRJET-ISMST17.pdf.
11. Alias AN, Zabidi ZM, Ali AMM, et al. Optical characterization and properties of polymeric materials for optoelectronic and photonic applications. International Journal of Applied Science and Technology. 2013; 3(5). Available online: https://www.researchgate.net/publication/290487984_Optical_characterization_and_properties_of_polymeric_materials_for_optoelectronic_and_photonic_applications.
12. Bourguiba F, Dhahri A, Tahri T, et al. Structural, optical spectroscopy, optical conductivity and dielectric properties of $BaTi_{0.5}(Fe_{0.33}W_{0.17})O_3$ perovskite ceramic. Bulletin of Materials Science. 2016; 39(7): 1765–1774. doi: 10.1007/s12034-016-1305-9.
13. Diatta A, Colin CV, Viennois R, et al. $BaCoO_2$ with Tetrahedral Cobalt Coordination: The Missing Element to Understand Energy Storage and Conversion Applications in $BaCoO_{3-\delta}$—Based Materials. Journal of the American Chemical Society. 2024; 146(22): 15027–15035. doi: 10.1021/jacs.3c14047.
14. Dubey DP, Chatterjee R. Magnetically tuned thermoelectric properties of metal-oxides: A review. Materials Research Express. 2024; 11(7): 072002. doi: 10.1088/2053-1591/ad6533.
15. Kim C, Kim S, Hong YK, et al. Correlation between the magnetic and thermoelectric properties in Mg_2−Mn Si. Journal of Alloys and Compounds. 2017; 690: 51–56. doi: 10.1016/j.jallcom.2016.08.095.
16. Rafiq F, Govindsamy P, Periyasamy S. Synthesis of a Novel Nanoparticle $BaCoO_{2.6}$ through Sol-Gel Method and Elucidation of Its Structure and Electrical Properties. Journal of Nanomaterials. 2022; 2022(1): 3877879. doi: 10.1155/2022/3877879.

17. Panigrahi SK, Tarai M. Derived UV–Vis Absorbance Spectra for Facile Analysis of Optically Dense Samples. ACS Omega. 2026; 11(13): 20136–20144. doi: 10.1021/acsomega.5c08711.
18. Valko M, Leibfritz D, Moncol J, et al. Free radicals and antioxidants in normal physiological functions and human disease. The International Journal of Biochemistry & Cell Biology. 2007; 39(1): 44–84. doi: 10.1016/j.biocel.2006.07.001.
19. Choi J, Qin W, Liu Mingfei, et al. Preparation and Characterization of $(La_{0.8}\ Sr_{0.2})_{0.95}MnO_{3-\delta}$ (LSM) Thin Films and LSM/LSCF Interface for Solid Oxide Fuel Cells. Journal of the American Ceramic Society. 2011; 94(10): 3340–3345. doi: 10.1111/j.1551-2916.2011.04614.x.
20. Sopicka-Lizer M, Smaczyński P, Kozłowska K, et al. Preparation and characterization of calcium cobaltite for thermoelectric application. Journal of the European Ceramic Society. 2005; 25(12): 1997–2001. doi: 10.1016/j.jeurceramsoc.2005.03.222.
21. Bhavsar V, Tripathi D. Study of refractive index dispersion and optical conductivity of PPy doped PVC films. Indian Journal of Pure and Applied Physics. 2016; 54(2). Available online: https://inis.iaea.org/records/wy8m2-tp254.
22. Agarwal S, Saraswat YK, Saraswat VK. Study of Optical Constants of ZnO Dispersed PC/PMMA Blend Nanocomposites. Open Physics Journal. 2016; 3(1): 63–72. doi: 10.2174/1874843001603010063.
23. Elthair NA, Mustafa EM, A. Elbadawi A. The Electrical and Optical Properties of $Zn_{0.5}Li_{2x}Mg_{0.5-x}Fe_2O_4$ Lithium Doped Nanoparticle Prepared by Coprecipitation Method. Open Journal of Applied Sciences. 2020; 10(09): 551–560. doi: 10.4236/ojapps.2020.109039.
24. Sharma N, Sharma S, Prabakar K, et al. Optical band gap and associated band-tails in nanocrystalline AlN thin films grown by reactive IBSD at different substrate temperatures. arXiv preprint. 2015. doi: 10.48550/ARXIV.1507.04867.
25. Najar FA, Vakil GB, Want B. Structural, optical and dielectric studies of lithium sulphate monohydrate single crystals. Materials Science-Poland. 2017; 35(1): 18–31. doi: 10.1515/msp-2017-0002.
26. Akhtar F, Podder J. A Study on Growth, Structural, Optical and Electrical Characterization of L-alanine Single Crystal for Optoelectronic Devices. Research Journal of Physics. 2012; 6(2): 31–40. doi: 10.3923/rjp.2012.31.40.
27. Suhail MH, Ahmed RA. Structural, optical and electrical properties of doped copper ZnS thin films prepared by chemical spray pyrolysis technique. Advances in Applied Science Research. 2014; 5(5): 139–147. Available online: https://www.primescholars.com/articles/avo-analysis-of-3d-seismic-data-at-gfield-norway.pdf.
28. Pavan Kumar CHSS, Pandeeswari R, Jeyaprakash BG. Structural, morphological and optical properties of spray deposited Mn-doped CeO_2 thin films. Journal of Alloys and Compounds. 2014; 602: 180–186. doi: 10.1016/j.jallcom.2014.02.143.
29. Ezeobele E, Ezenwa I. Optical Properties of Silver Aluminium Sulphide Ternary Thin Films Deposited by Chemical Bath Method. Afrrev Stech: An International Journal of Science and Technology. 1970; 4(1): 45–57. doi: 10.4314/stech.v4i1.5.
30. Basha B, Ghous A, Jamil A, et al. Structural, optical, and frequency dependent electric parameter and microwave absorbing properties of cobalt substituted barium aluminates prepared using a sol gel technique. Ceramics International. 2025; 51(25): 46237–46248. doi: 10.1016/j.ceramint.2025.07.331.
31. Pawar CS, Yadav AT, Salunkhe SP. Structural, Morphological, and Optical Properties of Cobalt Oxide Thin Films. Macromolecular Symposia. 2021; 400(1): 2100125. doi: 10.1002/masy.202100125.
32. Taha TA, Abouhaswa AS. Structure, optical and magnetic properties of barium sodium borate/cobalt oxide glass structures. Optical and Quantum Electronics. 2023; 55(6): 483. doi: 10.1007/s11082-023-04680-5.
33. Naz F, Saeed K. Synthesis of barium oxide nanoparticles and its novel application as a catalyst for the photodegradation of malachite green dye. Applied Water Science. 2022; 12(6): 121. doi: 10.1007/s13201-022-01649-9.
34. Elsammani AHA, Hamza HGI. Determination of the Optical Properties of Cobalt Oxide Using Ultraviolet Visible Spectroscopy. Bima Journal of Science and Technology. 2024; 8(3). Available online: https://journal-academia.com/Ojs/index.php/bimajst/article/view/762.
35. Faizee SAU, Nahire SB, Ahmed MTR. Spectral and Optical Analysis of Barium and Cobalt Oxides with Photocatalytic Insights. Journal of Nanoscience and Technology. 2026; 11(4): 1130. doi: 10.30799/jnst.S303.26110403.
36. Rafiq F, Jones S, Purushothaman P. Synthesis, and explication of structural and optical characteristics of $Ba_3Co_2O_6(CO_3)_{0.6}$. Next Materials. 2025; 8: 100573. doi: 10.1016/j.nxmate.2025.100573.
37. Paskaleva A, Spassov D, Terziyska P. Electric, dielectric and optical properties of Ga_2O_3 grown by metal organic chemical vapour deposition. Journal of Physics: Conference Series. 2017; 794: 012017. doi:

10.1088/1742-6596/794/1/012017.
38. Najeeb HN, Dahash GA, Haddawi SF, et al. Study of Changes in Optical Properties of PMMA Film before and after Irradiation by Laser. Chemical and Materials Engineering. 2014; 2(6): 145–147. doi: 10.13189/cme.2014.020603.
39. Eichhorn J, Lechner SP, Jiang CM, et al. Indirect bandgap, optoelectronic properties, and photoelectrochemical characteristics of high-purity Ta_3N_5 photoelectrodes. Journal of Materials Chemistry A. 2021; 9(36): 20653–20663. doi: 10.1039/D1TA05282A.
40. Bolarinwa HS, Onuu MU, Fasasi AY, et al. Determination of optical parameters of zinc oxide nanofibre deposited by electrospinning technique. Journal of Taibah University for Science. 2017; 11(6): 1245–1258. doi: 10.1016/j.jtusci.2017.01.004.
41. Muhammad FF, Yahya MY, Aziz F, et al. Tuning the extinction coefficient, refractive index, dielectric constant and optical conductivity of Gaq3 films for the application of OLED displays technology. Journal of Materials Science: Materials in Electronics. 2017; 28(19): 14777–14786. doi: 10.1007/s10854-017-7347-y.
42. Vinutha KV, Kumar KBK, Tejas MK, et al. Natural Dye Sensitized Solar Cells Using Anthocyanin Pigment Of Strawberry As Sensitizers. Imperial Journal of Interdisciplinary Research (IJIR). 2016; 2(10): 1011–1016. Available online: https://www.researchgate.net/publication/308368316_Natural_Dye_Sensitized_Solar_Cells_Using_Anthocyanin_Pigment_Of_Strawberry_As_Sensitizers.
43. Abu-Sehly AA. Optical constants and electrical conductivity of $Ge_{20}Se_{60}Sb_{20}$ thin films. Journal of Materials Science. 2000; 35(8): 2009–2013. doi: 10.1023/A:1004791124418.
44. Sharma P, Katyal SC. Determination of optical parameters of a-$(As_2Se_3)_{90}Ge_{10}$ thin film. Journal of Physics D: Applied Physics. 2007; 40(7): 2115–2120. doi: 10.88/0022-3727/40/7/038.
45. Barde NP, Rathod VR, Solanki PS, et al. On the structural, refractive index and energy bandgap based optical properties of Lithium ferrite nanoparticles dispersed in silica matrix. Applied Surface Science Advances. 2022; 11: 100302. doi: 10.1016/j.apsadv.2022.100302.
46. Lamichhane A. Energy-Gap-Refractive Index Relations in Semiconductors—Using Wemple–DiDomenico Model to Unify Moss, Ravindra, and Herve–Vandamme Relationships. Solids. 2023; 4(4): 316–326. doi: 10.3390/solids4040020.
47. Farag AAM, Yahia IS, AlFaify S, et al. Optical dispersion parameters based on single-oscillator model and optical absorption of nanocrystalline metal phthalocyanine films: A comparison study. Superlattices and Microstructures. 2013; 60: 83–100. doi: 10.1016/j.spmi.2013.04.018.
48. El Hamidi A, El Mahboub E, Meziane K, et al. The effect of electronegativity on optical properties of Mg doped ZnO. Optik. 2021; 241: 167070. doi: 10.1016/j.ijleo.2021.167070.
49. Dhineshbabu NR, Rajendran V, Nithyavathy N, et al. Study of structural and optical properties of cupric oxide nanoparticles. Applied Nanoscience. 2016; 6(6): 933–939. doi: 10.1007/s13204-015-0499-2.
50. Choudhury B, Choudhury A. Oxygen defect dependent variation of band gap, Urbach energy and luminescence property of anatase, anatase–rutile mixed phase and of rutile phases of TiO_2 nanoparticles. Physica E: Low-dimensional Systems and Nanostructures. 2014; 56: 364–371. doi: 10.1016/j.physe.2013.10.014.
51. Gherasim C, Asandulesa M, Fifere N, et al. Structural, Optical and Dielectric Properties of Some Nanocomposites Derived from Copper Oxide Nanoparticles Embedded in Poly (vinylpyrrolidone) Matrix. Nanomaterials. 2024; 14(9): 759. doi: 10.3390/nano14090759.
52. El Bachiri A, Soussi L, Karzazi O, et al. Electrochromic and photoluminescence properties of cobalt oxide thin films prepared by spray pyrolysis. Spectroscopy Letters. 2019; 52(1): 66–73. doi: 10.1080/00387010.2018.1556221.
53. Singh P, Sharma P, Sharma V, et al. Linear and non-linear optical properties of Ag-doped $Ge_2Sb_2Te_5$ thin films estimated by single transmission spectra. Semiconductor Science and Technology. 2017; 32(4): 045015. doi: 10.1088/1361-6641/aa5ee0.
54. Usman A, Halimah MK, Latif AA, et al. Influence of Ho^{3+} ions on structural and optical properties of zinc borotellurite glass system. Journal of Non-Crystalline Solids. 2018; 483: 18–25. doi: 10.1016/j.jnoncrysol.2017.12.040.
55. Rathore MS, Verma H, Akhani SB, et al. Photoluminescence and antibacterial performance of sol–gel synthesized ZnO nanoparticles. Materials Advances. 2024; 5(8): 3472–3481. doi: 10.1039/D3MA01096A.
56. Saikia L, Bhuyan D, Saikia M, et al. Photocatalytic performance of ZnO nanomaterials for self sensitized degradation of malachite green dye under solar light. Applied Catalysis A: General. 2015; 490: 42–49. doi: 10.1016/j.apcata.2014.10.053.
57. Gancheva M, Iordanova R, Koseva I, et al. Synthesis and Luminescent Properties of Barium Molybdate Nanoparticles.

Materials. 2023; 16(21): 7025. doi: 10.3390/ma16217025.
58. Zhao JH, Liu CJ, Lv ZH. Photoluminescence of ZnO nanoparticles and nanorods. Optik. 2016; 127(3): 1421–1423. doi: 10.1016/j.ijleo.2015.11.018.
59. Fulati R, Dai P. The Phase Transition and Photoluminescence Properties of $(Ca_{9-x}Sr_x)Mg_{1.5}(PO_4)_7$: Eu^{2+} Solid-Solution Phosphors. ECS Journal of Solid State Science and Technology. 2021; 10(3): 036005. doi: 10.1149/2162-8777/abefae.
60. de Passos C, Merchán MD, Velázquez MM. Correlations between structure and photoluminescence properties in N-doped carbon nanoparticles. Journal of Science: Advanced Materials and Devices. 2022; 7(1): 100408. doi: 10.1016/j.jsamd.2021.100408.
61. Huang CY, Chatterjee A, Liu SB, et al. Photoluminescence properties of a single tapered CuO nanowire. Applied Surface Science. 2010; 256(11): 3688–3692. doi: 10.1016/j.apsusc.2010.01.007.
62. Wang T, Zheng M, Wang Z, et al. Luminescence and energy transfer of single-phase white-emitting phosphor $Ba_2Mg(PO_4)_2$: Ce^{3+}, Eu^{2+} for white LEDs. RSC Advances. 2022; 12(53): 34404–34413. doi: 10.1039/D2RA06357C.
63. Dawar N, Chitkara M, Sandhu IS, et al. Structural, magnetic and dielectric properties of pure and nickel-doped barium nanohexaferrites synthesized using chemical co-precipitation technique. Cogent Physics. 2016; 3(1). doi: 10.1080/23311940.2016.1208450.
64. Rahman KR, Chowdhury FUZ, Khan MNI. Structural, morphological and magnetic properties of Al^{3+} substituted $Ni_{0.25}Cu_{0.20}Zn_{0.55}AlxFe_{2-x}O_4$ ferrites synthesized by solid state reaction route. Results in Physics. 2017; 7: 354–360. doi: 10.1016/j.rinp.2016.12.045.
65. Martins C, Rolo C, Cacho VRG, et al. Enhancing the magnetic properties of superparamagnetic iron oxide nanoparticles using hydrothermal treatment for magnetic hyperthermia application. Materials Advances. 2025; 6(5): 1726–1743. doi: 10.1039/D4MA01120A.
66. Myrovali E, Maniotis N, Makridis A, et al. Arrangement at the nanoscale: Effect on magnetic particle hyperthermia. Scientific Reports. 2016; 6(1): 37934. doi: 10.1038/srep37934.
67. Omelyanchik A, Salvador M, D'Orazio F, et al. Magnetocrystalline and Surface Anisotropy in $CoFe_2O_4$ Nanoparticles. Nanomaterials. 2020; 10(7): 1288. doi: 10.3390/nano10071288.
68. Salaheldeen M, Wederni A, Ipatov M, et al. Enhancing the Squareness and Bi-Phase Magnetic Switching of Co_2FeSi Microwires for Sensing Application. Sensors. 2023; 23(11): 5109. doi: 10.3390/s23115109.
69. Kaiser M. Effect of lanthanide and transition metal on the structure, magnetic, and electric properties of nickel ferrites. Applied Physics A. 2023; 129(12): 840. doi: 10.1007/s00339-023-07082-2.
70. Ahmad N, Jafri Z, Khan ZH. Evaluation of nanomaterials to prevent oral Candidiasis in PMMA based denture wearing patients. A systematic analysis. Journal of Oral Biology and Craniofacial Research. 2020; 10(2): 189–193. doi: 10.1016/j.jobcr.2020.04.012.
71. Benjamin SR, Lima FD, Florean EOPT, et al. Current trends in nanotechnology for bioremediation. International Journal of Environment and Pollution. 2019; 66(1/2/3): 19. doi: 10.1504/IJEP.2019.104526.
72. Samaranayake L, Parahitiyawa N. Oral Medicine and Pathology: A Guide to Diagnosis and Management. In: Infections of the Oral Mucosa. Jaypee; 2014.
73. Meran Z, Besinis A, de Peralta T, et al. Antifungal properties and biocompatibility of silver nanoparticle coatings on silicone maxillofacial prostheses in vitro. Journal of Biomedical Materials Research Part B: Applied Biomaterials. 2018; 106(3): 1038–1051. doi: 10.1002/jbm.b.33917.
74. Sonnahalli NK, Chowdhary R. Effect of adding silver nanoparticle on physical and mechanical properties of maxillofacial silicone elastomer material-an in-vitro study. Journal of Prosthodontic Research. 2020; 64(4): 431–435. doi: 10.1016/j.jpor.2019.12.001.
75. Babayevska N, Przysiecka Ł, Iatsunskyi I, et al. ZnO size and shape effect on antibacterial activity and cytotoxicity profile. Scientific Reports. 2022; 12(1): 8148. doi: 10.1038/s41598-022-12134-3.
76. Yue L, Asim MH, Alamgeer, et al. Recent Development on Application of Nanomaterials-Based Antibacterial Nanoparticles Against Oral Infections: A Comprehensive Review. ChemistrySelect. 2025; 10(27): e01546. doi: 10.1002/slct.202501546.
77. Alshemary AZ, Goh YF, Akram M, et al. Barium and Fluorine Doped Synthetic Hydroxyapatite: Characterization and In-Vitro Bioactivity Analysis. Science of Advanced Materials. 2015; 7(2): 249–257. doi: 10.1166/sam.2015.2103.
78. Huang X, He D, Pan Z, et al. Reactive-oxygen-species-scavenging nanomaterials for resolving inflammation. Materials Today Bio. 2021; 11: 100124. doi: 10.1016/j.mtbio.2021.100124.

79. Djurišić AB, Leung YH, Ng AMC, et al. Toxicity of Metal Oxide Nanoparticles: Mechanisms, Characterization, and Avoiding Experimental Artefacts. Small. 2015; 11(1): 26–44. doi: 10.1002/smll.201303947.
80. Bankar N, Latta L, Loretz B, et al. Antimicrobial and antibiotic-potentiating effect of calcium peroxide nanoparticles on oral bacterial biofilms. Biofilms and Microbiomes. 2024; 10(1): 106. doi: 10.1038/s41522-024-00569-7.